$$\begin{bmatrix} U^{n+1}_{I,J,K} \\ U^{n+1}_{I,J+1,K} \\ U^{n+1}_{I,J+2,K} \end{bmatrix} = \begin{bmatrix} 0 & [A^{+1y}_{u}]_{I,J,K} & [A^{+2y}_{u}]_{I,J,K} \\ 0 & 1 & 0 \\ 0 & 0 & 1 \end{bmatrix} \begin{bmatrix} u^{n+1}_{I,J,K} \\ u^{n+1}_{I,J+1,K} \\ u^{n+1}_{I,J+2,K} \end{bmatrix}. \tag{52}$$

Eq. (52) represents a forcing at a grid point (I,J,K), and the 3×3 matrix in the right-hand side is a minimum sub-matrix to compose a full matrix for the three-dimensional space. For the sub-matrix $\mathcal{E}$, the satisfaction of $\mathcal{E}=\mathcal{E}^2$ can be easily confirmed. If the full matrix is composed of this minimum sub-matrix, the forcing strategy conserves the order of the temporal accuracy. We show next a forcing strategy decreasing the accuracy. The example is shown as

$$\begin{bmatrix} U^{n+1}_{I,J,K} \\ U^{n+1}_{I,J+1,K} \\ U^{n+1}_{I,J+2,K} \\ U^{n+1}_{I,J+3,K} \end{bmatrix} = \begin{bmatrix} 0 & [A^{+1y}_{u}]_{I,J,K} & [A^{+2y}_{u}]_{I,J,K} & 0 \\ 0 & 0 & [A^{+1y}_{u}]_{I,J+1,K} & [A^{+2y}_{u}]_{I,J+1,K} \\ 0 & 0 & 1 & 0 \\ 0 & 0 & 0 & 1 \end{bmatrix} \begin{bmatrix} u^{n+1}_{I,J,K} \\ u^{n+1}_{I,J+1,K} \\ u^{n+1}_{I,J+2,K} \\ u^{n+1}_{I,J+3,K} \end{bmatrix}. \tag{53}$$

In this equation, one forcing velocity $U^{n+1}_{I,J+1,K}$ is used for interpolating the other velocity $U^{n+1}_{I,J,K}$. We call this an overlapped forcing, which leads to $\mathcal{E}\neq\mathcal{E}^2$. If the full matrix includes this sub-matrix, the forcing strategy diminishes the order of the temporal accuracy.

4. Numerical examples

4.1. Flow in a planar channel

4.1.1. Computational setups

Flow in a planar channel is chosen to verify the consistent scheme for the no-slip wall condition. The fractional step method represented by Eqs. (29)–(31) is used. LES with the no-slip condition is performed for a developed turbulent flow, where the Reynolds number, based on the channel half width L and the bulk velocity u_m, is approximately 5×10^3. Smagorinsky model is used with van Driest damping function. The Reynolds number, based on the friction velocity u_T and the channel half width L, is 180.

The computational domain for planar channel is shown in Fig. 6. As shown in Fig. 6a, the channel wall is represented by the solid objects and the wall is inclined to the computational grid system $O-xyz$. To explain computational results for the inclined channel, the coordinate system $O-x'y'z$ with the x'-axis in the mainstream direction and the y'-axis in the wall normal direction is introduced. The main flow is maintained by a mean pressure gradient in the x'-direction. As shown in Fig. 6b, the inclination of the wall is set at approximately $\theta=0°$, 5°, 10° and 20° so that the wall locates on the cell vertices. This setup allows the periodical boundary condition for the mainstream and has benefits for spatial average in turbulent flow calculations and for checking directly the computed velocity on the grid point.

4.1.2. Aligned channel

In order to compare the results between the immersed boundary method and the body fitted method with the same grid arrangement, the walls are located on the Cartesian grid line by setting $\theta=0°$ as shown in Fig. 6b. This setup enables us to confirm the realizability of the wall condition shown in Table 1. In this computation, only the coefficients $A^{\pm 2y}_{u_i}$ and $A^{\pm 1y}_{u_i}$ are used in Eq. (25). Since $A^{+1y}_{u}=A^{+1y}_{w}$, the extra terms explained in the Section 3.2 are canceled in a laminar flow because of $v_{I,J+1,K}=v_{I,J,K}=0$. Moreover, since $(1+A^{+1y}_{u}-A^{+1y}_{v})/A^{+1y}_{u}=4(\because d^{y}_{u}=0)$, they are canceled in a turbulent flow if the asymptotical behavior $(v_{I,J+1,K}=4v_{I,J,K})$ is reproduced. The satisfaction of $\mathrm{div}\,\mathbf{u}=0$ and $\mathbf{u}\cdot\mathbf{n}=0$ is thus an evidence for that of $\mathbf{u}\times\mathbf{n}=0$, and therefore the satisfaction of the no-slip condition can be checked although the streamwise component u is not located on the wall.

First, LES of a fully developed turbulent flow is performed to verify the availability of the two-points forcing explained in the Section 2.2. No wall condition for the pressure equation is given as a preliminary step (corresponding to Case-B stated in the Section 3.1). After the flow reaches a fully developed state, 512 flow

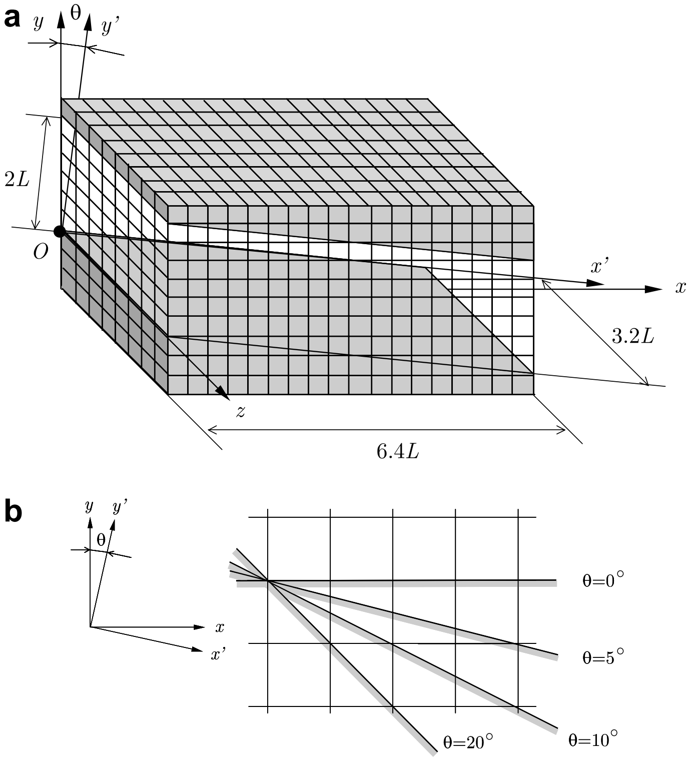

Fig. 6. The computational domain for planar channel: (a) grid and channel and (b) setups of wall inclination.

fields are averaged during $5t^*$, where t^* is the dimensionless time normalized by L/u_T. The number of grids used in the fluid region is changed as $32 \times 30 \times 32$, $64 \times 60 \times 64$, $64 \times 120 \times 64$ and $64 \times 240 \times 64$ to investigate the convergence rate of spatial discrete error. In this regard, the grid number in the y-direction is changed to investigate the effect of the interpolation for immersed boundary. The successive over relaxation (SOR) method is used to solve Eqs. (29) and (31). The iteration is continued for the error to converge within 1×10^{-5} for Eq. (29) and 1×10^{-3} for Eq. (31). The error is defined by

$$\mathrm{Error} = \sqrt{\sum_{k=1}^{N} (X_k - Y_k)^2 \Big/ \sum_{k=1}^{N} Y_k^2}, \tag{54}$$

where N is total number of the data; X_k and Y_k are the left-hand and right-hand sides of equation, respectively. Fig. 7 shows the convergence of the error for different forcing methods. The error is defined by Eq. (54), where X_k and $Y_k (k = 1, 2, \ldots, N_y$, N_y: number of grid points in the y-direction) are the mean axial velocities by the immersed boundary method (IBM) and the body fitted method (BFM), respectively. The error is evaluated at each number of grids to eliminate the effect of grid resolution on Smagorinsky model and to emphasize the difference in the wall treatment. In this figure, the two-points forcing method (2P-Linear) are compared with the one-point forcing in the fluid region using linear interpolation (1P-Linear) and that using the second-order Lagrange interpolation (1P-Lagrange). The figure indicates that these three methods are second-order accuracy and no significant problem arises. However, as shown in Fig. 8, the divergence free condition is seriously affected by the forcing method. Here, $|\mathrm{div}\,\mathbf{u}|$ is evaluated at the cell closest to the wall using Eq. (8) normalized by the bulk velocity. The error for the one-point forcing methods (1P-Linear and 1P-Lagrange) does not converge whereas that for the two-points forcing method (2P-Linear) maintains second-order accuracy. The result indicates that introducing the present two-points forcing method is more practical than developing the interpolation order for the one-point forcing.

Next, to verify the consistent scheme explained in Section 2.3, LES by the schemes of Cases A, B and C explained in Section 3.1 are carried out using $32 \times 30 \times 32$ grids in the fluid region. The values of instantaneous

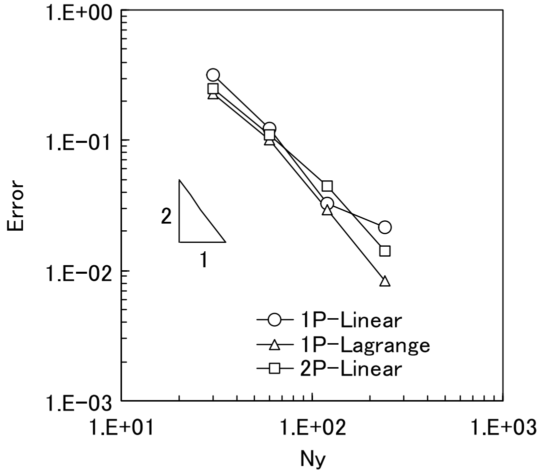

Fig. 7. Convergence of the error in mean streamwise velocity for different forcing methods (aligned channel).

velocity and its divergence in a cell adjacent to the wall are shown in Table 2. The arrangement of velocities in the cell are shown in Fig. 9. In the table, $\mathrm{div}\,\mathbf{u}$ is calculated by Eq. (8) as

$$\mathrm{div}\,\mathbf{u} = \frac{U_{I,J,K} - U_{I-1,J,K}}{h_x} + \frac{v_{I,J,K} - V_{I,J-1,K}}{h_y} + \frac{W_{I,J,K} - W_{I,J,K-1}}{h_z}, \tag{55}$$

where remind that the capital letter indicates a forcing velocity. The result reasonably reproduces the conservation property theoretically predicted in Sections 3.1 and 3.2. Namely, the wall condition is satisfied ($V_{I,J-1,K} = 0$) in Cases A and C, but the divergence free condition is unsatisfied ($\mathrm{div}\,\mathbf{u} \neq 0$) in Case-C. In Case-B, the divergence free condition is satisfied ($\mathrm{div}\,\mathbf{u} = 0$) but the wall condition is unsatisfied ($V_{I,J-1,K} \neq 0$). Here, the non-zero value of $\mathrm{div}\,\mathbf{u}$ for Case-B is caused by the truncation error with the digits shown in the table. Thus, only Case-A can satisfy both the wall condition and the divergence free condition.

It is noted that the drawback of Cases B and C becomes obvious in the turbulent flow simulation. For example, the velocity profile for the laminar flow indicates no significant difference among Cases A, B and C, as shown Fig. 10, and we were not able to find the drawback in the digits like those shown in Table 2. To observe the detail, the convergence of the error in divergence free condition as a function of the error in the pressure equation is shown in Fig. 11. The divergence of velocity is normalized by bulk velocity and

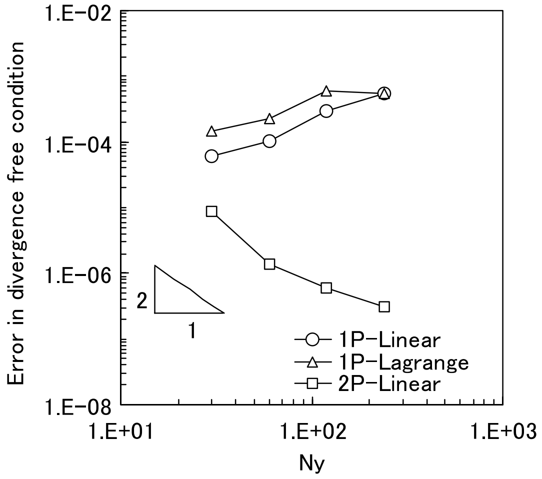

Fig. 8. Convergence of the error in divergence free condition for different forcing methods (aligned channel).

Table 2
Instantaneous velocity and divergence in the forcing cell (aligned channel, 32 × 30 × 32 grids, the values are normalized by u_T for velocity and L for length)

Case	$U_{I-1,J,K}$	$U_{I,J,K}$	$V_{I,J-1,K}$	$v_{I,J,K}$	$W_{I,J,K-1}$	$W_{I,J,K}$	div**u**
A	3.52975	3.85343	0.00000	−0.00552	0.14868	−0.30224	0.00000
B	4.02783	3.91385	−0.10305	0.06124	0.06600	−0.12346	0.00020
C	3.07369	3.45770	0.00000	0.08751	0.27085	−0.05553	−0.06194

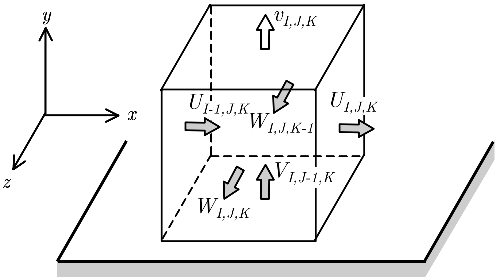

Fig. 9. The forcing velocities in the aligned channel.

mean grid spacing $\Delta = (h_x h_y h_z)^{1/3}$. The figure shows that the error for Cases A and B converges as the error in the pressure equation approaches the machine-zero, while that for Case-C does not converge. Remind that the wall condition is broken in Case-B. In the laminar flow simulation, the drawback of the conventional immersed boundary method thus appears in the error acceptably small. We should remark that the consistency pointed in this study is important for the turbulence simulation in industry, where using coarse mesh is sometimes inevitable.

4.1.3. Inclined channel

The flow with the wall inclined to the Cartesian grid system is simulated. The grid number kept in the channel is 32 × 30 × 32 for the x, y and z directions, and the total grid number is changed as 32 × 40 × 32, 32 × 48 × 32 and 32 × 64 × 32 to simulate $\theta = 5°,10°$ and 20° inclinations, respectively. In this computation, the coefficients $A_{u_i}^{\pm 2x}$, $A_{u_i}^{\pm 2y}$, $A_{u_i}^{\pm 1x}$ and $A_{u_i}^{\pm 1y}$ are used in Eq. (25).

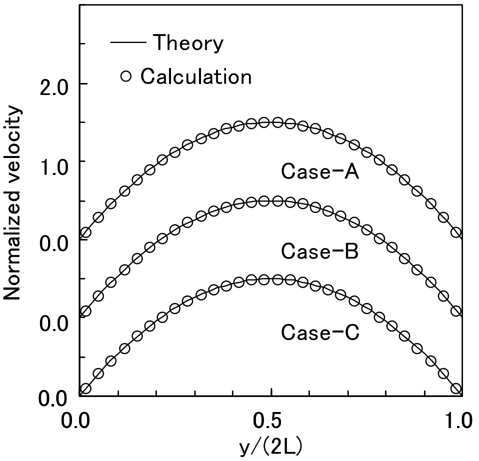

Fig. 10. Velocity profile (u_x/u_m) in the laminar flow: comparison with theory ($u = 3u_m(2Ly - y^2)/(2L^2)$) (aligned channel, 32 × 30 × 32 grids).

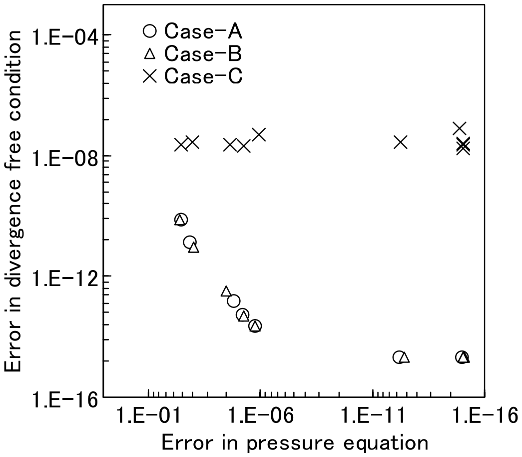

Fig. 11. Error of divergence free condition in the laminar flow (aligned channel, 32 × 30 × 32 grids).

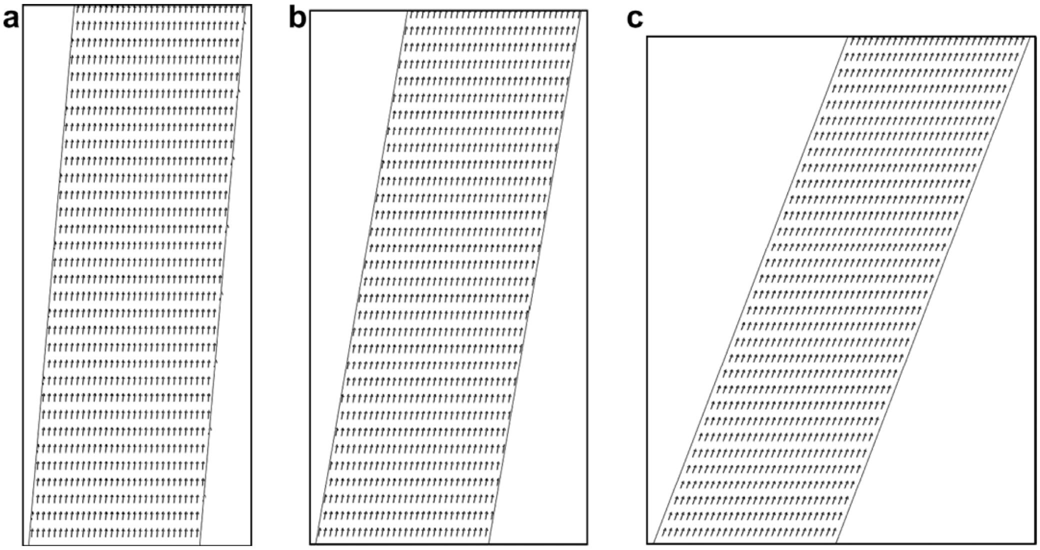

Fig. 12. Velocity vectors $(u_{x'}, u_{y'})$ with uniform length in the laminar flow for $\theta =$ (a) 5°, (b) 10° and (c) 20° (inclined channel, immersed boundary method, 32 × 48 × 32 grids, plotted on every grid point).

First, to compare with the theory, the laminar flow is simulated for the inclination of $\theta = 5°,10°$ and 20°. The velocity vector and profile obtained by the present immersed boundary method are shown in Figs. 12 and 13. In Fig. 12, the vector is indicated with a uniform length independently of its value, to highlight the velocity calculated in near-wall region. In Fig. 13, velocity profiles at the inlet, the outlet and the midpoint ($I = 1$, 32 and 16) all agree well with the theory. In Figs. 14 and 15, the results by the stair-steps approximation, where velocities are set as zero in the cell nearest to the wall, are shown. The flow near the wall is disturbed and the flow rate in the channel is decreased. The present immersed boundary method is advantageous for representing the wall inclined to the Cartesian grid system.

Next, to investigate the temporal accuracy of the present scheme, LES of a fully developed turbulent flow is performed. The inclination of $\theta = 10°$ is chosen because both overlapped forcing and non-overlapped forcing are included. The arrangement of velocities in the cell are shown in Fig. 16. The forcing velocities $V_{I,J}$ and $V_{I+1,J}$ are overlapped and non-overlapped, respectively. The forcing velocity $V_{I,J}$ is interpolated using $v_{I,J+1}$

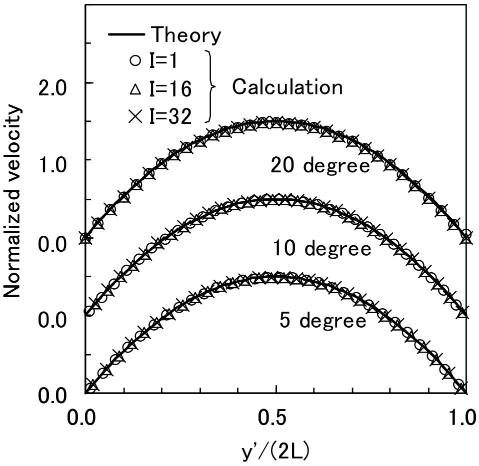

Fig. 13. Velocity profile ($u_{x'}/u_m$) in the laminar flow: comparison with theory ($u = 3u_m(2Ly' - y'^2)/(2L^2)$) (inclined channel, immersed boundary method, $32 \times 48 \times 32$ grids).

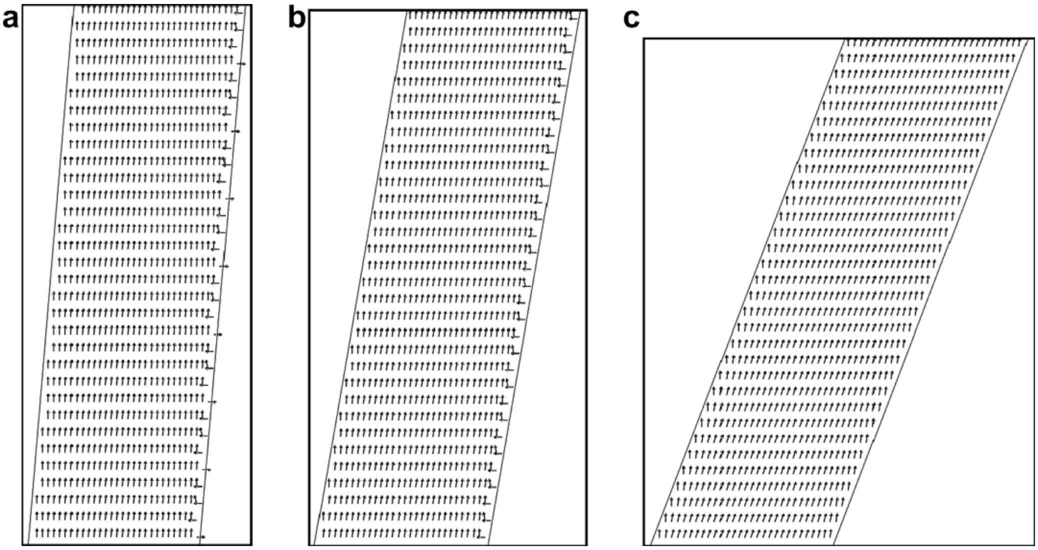

Fig. 14. Velocity vectors ($u_{x'}, u_{y'}$) with uniform length in the laminar flow for θ = (a) 5°, (b) 10° and (c) 20° (inclined channel, stair-step approximation, $32 \times 48 \times 32$ grids, plotted on every grid point).

in the y-direction and $V_{I+1,J}$ in the x-direction whereas the forcing velocity $V_{I+1,J}$ is interpolated using $v_{I+1,J+1}$ only in the y-direction.

Simulations are performed for several Δt, and 1000 velocities are averaged during $10t^*$ after the flow is developed. The iteration in the SOR method for Eq. (29) and Eq. (31) is continued for the error defined by Eq. (54) to converge within 1×10^{-5}. The convergence to the divergence free condition are therefore maintained independently of Δt. As discussed in the Section 3.2, the divergence free condition is satisfied in the cell $(I+1, J+1)$ but the cell $(I, J+1)$ because the former includes only one forcing velocity whereas the latter does two forcing velocities in different coordinate directions. Actually, in these simulations, the divergence of velocity $[\mathrm{div}\,\mathbf{u}]_{I+1,J+1}$ and $[\mathrm{div}\,\mathbf{u}]_{I,J+1}$, normalized by u_T and P, is approximately 10^{-4} and 10^{+1}, respectively.

L_∞ and L_2 errors are determined from a reference mean velocity field obtained at a minimum time spacing $\Delta t = 1.25 \times 10^{-4}\ t^*$, where the Courant number based on the fluctuating velocity and the mean grid spacing is

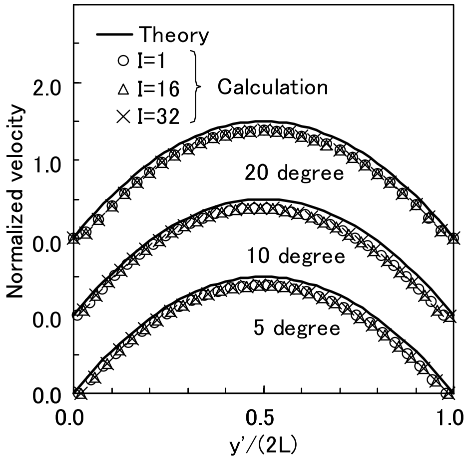

Fig. 15. Velocity profile $(u_{x'}/u_m)$ in the laminar flow: comparison with theory $(u = 3u_m(2Ly' - y'^2)/(2L^2))$ (inclined channel, stair-step approximation, $32 \times 48 \times 32$ grids).

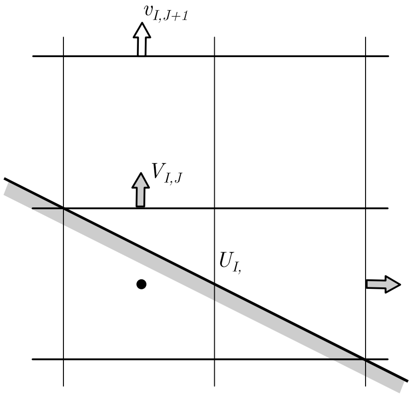

0.05. The L_∞ error is evaluated for $V_{I,J}$ (OV: overlapped) and $V_{I+1,J}$ (NOV: non-overlapped), and the L_2 error based on Eq. (54) is evaluated for mean streamwise velocity profile.

The temporal convergence obtained is shown in Fig. 17. The L_∞ error of OV certainly indicates lower order than that of NOV. The decrease however is insignificant, and both OV and NOV indicate generally second-order accuracy. On the other hand, the L_2 error of the inclined channel indicates the first-order as well as that of the aligned channel that does not include the overlapped forcing. This accuracy, the first-order, is caused by the factorization error, which was independent of boundary conditions in the body fitted method [9].

As the result indicates, in the immersed boundary method, the forcing velocity to represent the wall condition has discrete error relating to the temporal accuracy. The effect however is local as the delta function in Eq. (51) indicates.

4.2. Flow in a circular pipe

Flow in a circular pipe is chosen to verify the consistent scheme in a curved two-dimensional geometry. The fractional step method represented by Eqs. (32)–(34) is used. LES with the no-slip condition is performed for a developed turbulent flow, where the Reynolds number, based on the pipe diameter D and the bulk velocity u_m, is approximately 5×10^3.

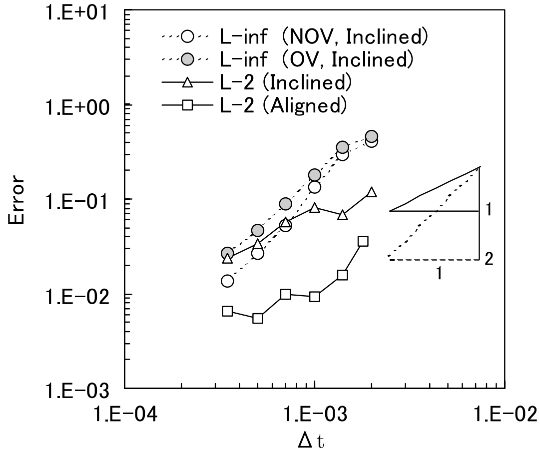

Fig. 17. Temporal convergence of the L_∞ error (L-inf) for the overlapped forcing (OV) and the non-overlapped forcing (NOV) velocities and L_2 error (L-2) for the streamwise velocity distribution (inclined channel, $32 \times 48 \times 32$ grids).

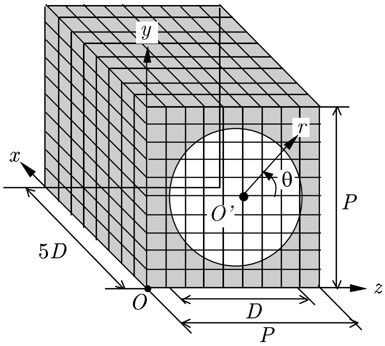

Fig. 18. Computational domain for circular pipe.

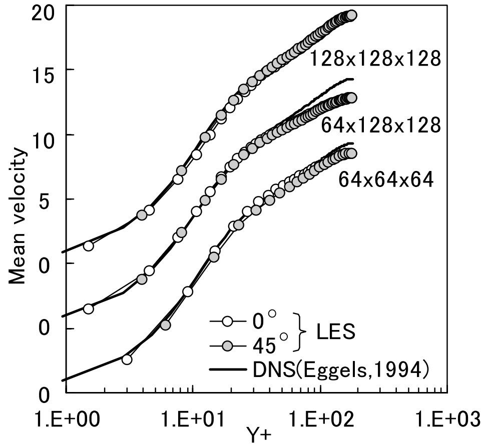

Fig. 19. Mean velocity ($\overline{u_x}/u_T$) in the turbulent flow (circular pipe, $Re_T = 360$).

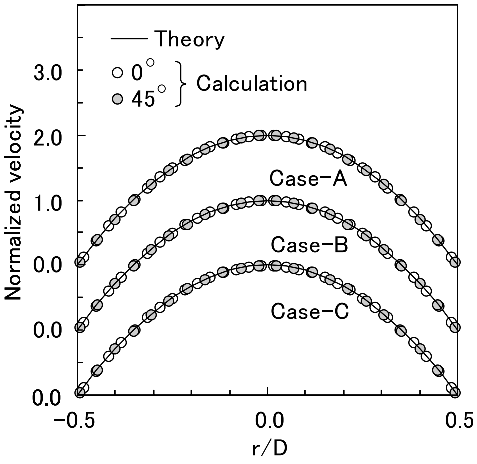

Fig. 20. Velocity profile (u_x/u_m) in the laminar flow: comparison with theory ($u = 2u_m(1 - 4r^2/D^2)$) (circular pipe, 32 × 32 × 32 grids).

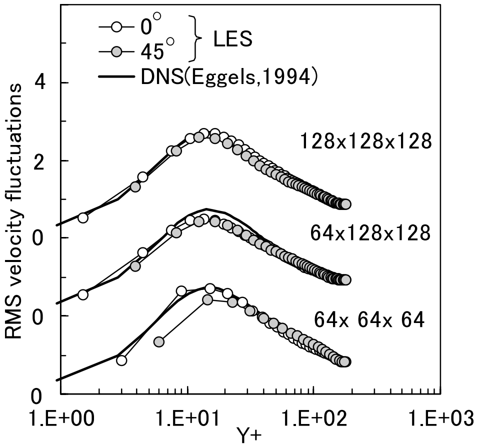

Fig. 21. RMS of velocity fluctuation $\left(\sqrt{\overline{u_x'^2}}/u_T\right)$ in the turbulent flow (circular pipe, $Re_T = 360$).

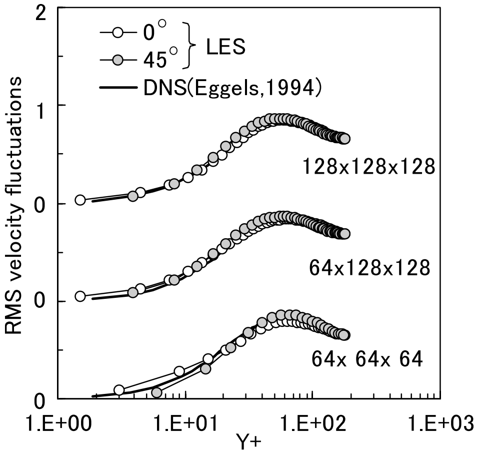

Fig. 22. RMS of velocity fluctuation $\left(\sqrt{\overline{u_r'^2}}/u_T\right)$ in the turbulent flow (circular pipe, $Re_T = 360$).

The computational domain is shown in Fig. 18. The main flow is maintained by a mean pressure gradient in the x-direction. In this computational domain, the coefficients $A_{u_i}^{\pm 2y}$, $A_{u_i}^{\pm 2z}$, $A_{u_i}^{\pm 1y}$ and $A_{u_i}^{\pm 1z}$ are used in Eq. (25). Hereinafter, the distance from the wall is defined by $Y = D/2 - r$. The result of LES is compared with that of DNS [15]. Smagorinsky model is used with van Driest damping function. The Reynolds number Re_T, based on the friction velocity u_T and the pipe diameter D, is 360. After the flow is developed, 800 flow fields are averaged during $4t^*$, where t^* is the dimensionless time normalized by D/u_T. Here, $D = 0.9375P$. The number of grids used in the whole domain is changed as $64 \times 64 \times 64$, $64 \times 128 \times 128$ and $128 \times 128 \times 128$ to show the conver-

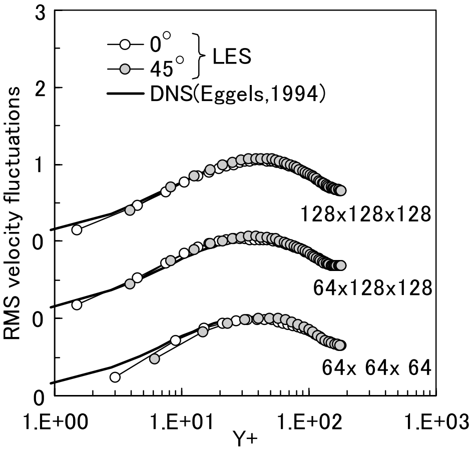

Fig. 23. RMS of velocity fluctuation $\left(\sqrt{\overline{u_\theta'^2}}/u_T\right)$ in the turbulent flow (circular pipe, $Re_T = 360$).

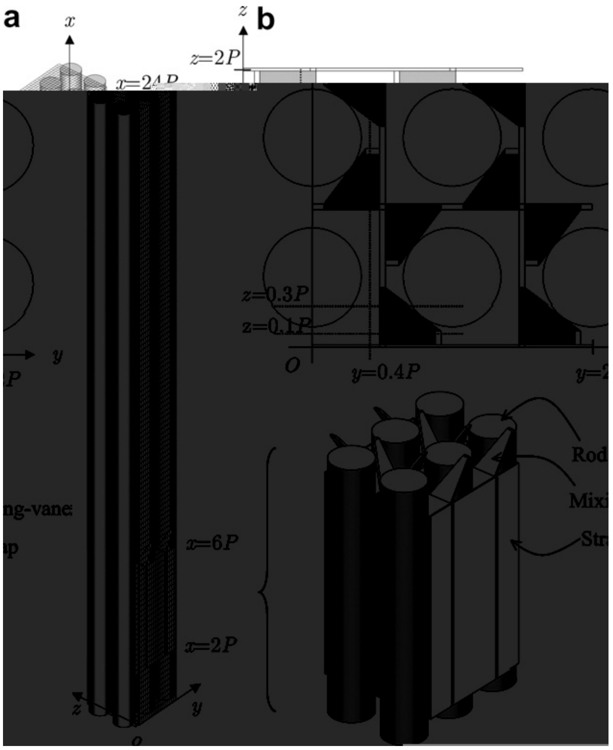

Fig. 24. The configuration of the rod bundle: (a) the computational domain and a part of grids; (b) the configuration of spacer.

gence of spatial discrete error. The iteration in the SOR method for Eqs. (32) and (34) is continued for the error defined by Eq. (54) to converge within 1×10^{-5}.

The mean streamwise velocity obtained by the LES is shown in Fig. 19. An azimuthal dependence appears between 0° and 45° for $64 \times 64 \times 64$, and it disappears for $64 \times 128 \times 128$ and $128 \times 128 \times 128$. To consider this, the result of the laminar flow simulation for this geometry is shown in Fig. 20. In this figure, the results for the schemes Case A, B and C, explained in Section 3.1, are shown and each of them is compared between 0° and 45°. The difference between 0° and 45° is insignificant independently of those schemes. As discussed for the planar channel in Section 4.1.2, the drawback of Case B and C was unapparent in the laminar flow because of no velocity fluctuation, and so is for this geometry. Since the wall condition is simulated thus reasonably, the azimuthal dependence in Fig. 19 is therefore caused by an asymmetry of the turbulent stresses, which are sensitive to the computational grid resolution. This is supported by the result for root mean square (RMS) of velocity fluctuation shown in Figs. 21–23. The tendency has appeared straightforward in the pipe geometry because of its complete axisymmetry. In a general complex configuration however, specifying the tendency is difficult and then it will cause a numerical uncertainty. Checking the grid resolution systematically is always important in spite of the coordinate system. The Cartesian coordinate has a benefit for systematically changing the grid resolution.

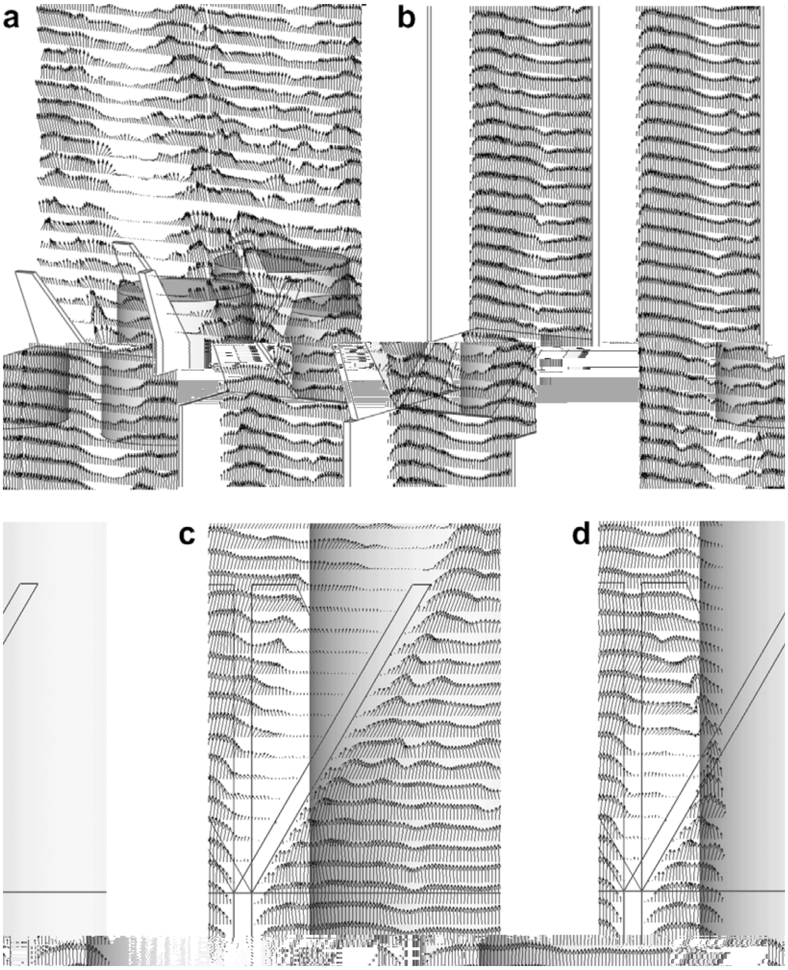

Fig. 25. Instantaneous velocities around the spacer: (u, v, w) at (a) the top and (b) the bottom at $y = 0.4P$ (plotted on every 2nd grid point); (u, v) at (c) $z = 0.1P$ and (d) $z = 0.3P$ (plotted on every grid point).

4.3. Flow in a nuclear rod-bundle

The present immersed boundary method is applied to a complex three-dimensional geometry of a nuclear rod-bundle. The fractional step method represented by Eqs. (29)–(31) is used. LES with the no-slip condition is performed for a developed turbulent flow, where the Reynolds number, based on the rod pitch P and the bulk velocity u_m, is approximately 4×10^3.

The rod-bundle is equipped with spacers designed to enhance heat transfer in a nuclear reactor core. Fig. 24 indicates the configuration of the rod-bundle by showing a typical part with a spacer. The reactor core is about 8 times the part in the length direction and 30 times that in the lateral direction. To simulate the flow in the reactor core, periodic boundary condition is given in the every coordinate direction to the computational domain shown in Fig. 24a. Mixing-vanes attached at the spacer, as shown in Fig. 24b, produces lateral flows by distorting the mainstream parallel to the bundled rods. Generating a body fitted structured grid for this configuration is difficult because the unit channel surrounded by 4 rods has a singular point in the channel center as well as the geometrical complexity of the spacer with the mixing-vanes. The rod-bundle geometry is therefore one of the best examples where the immersed boundary method is useful.

In this computation, the coefficients in Eq. (25) are all used. The configuration includes a corner of straps and a thin solid of the mixing-vane. Even if the corner locates within a cell, without changing the forcing algorithm the forcing velocity is given at the staggered points, and then the corner is approximated as a slope intersecting the cell. On the other hand, if the thin solid is within a cell, the forcing inside the body region is omitted to avoid disturbing the velocity field in the opposite.

The Reynolds number, based on the rod pitch P and the friction velocity averaged in the unit channel u_T, is 580. A one equation dynamic sub-grid scale model [16] is used. The number of grids used in the whole domain

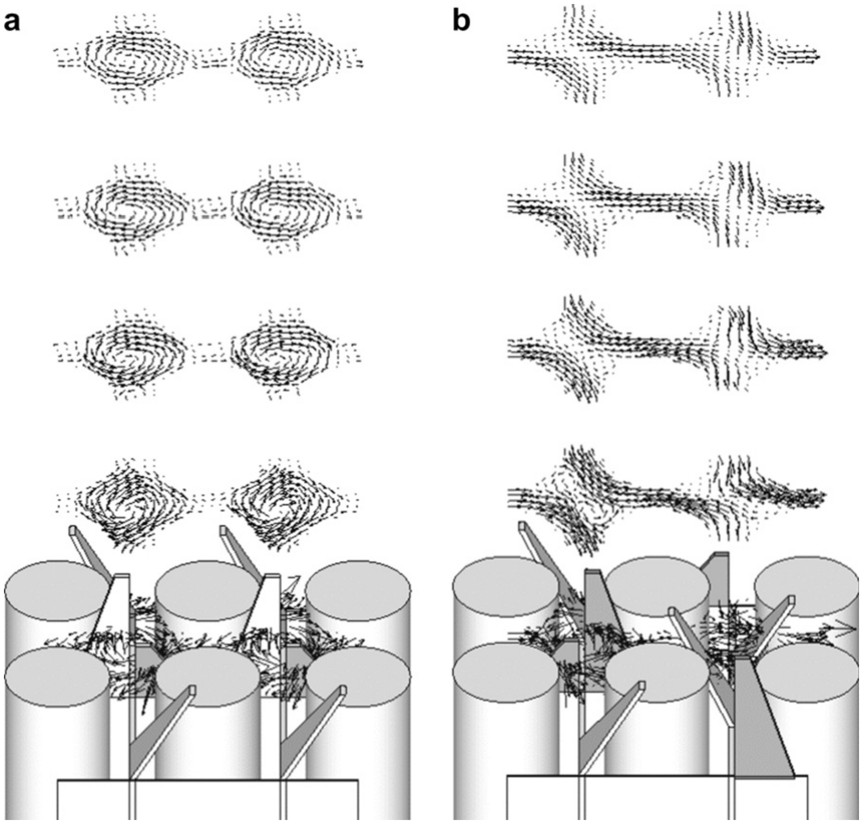

Fig. 26. Lateral flows (v, w) downstream from the spacers: (a) swirling flow and (b) crossing flow at $x = 6.4P$, $7.5P$, $8.6P$, $9.7P$ and $10.9P$ (plotted on every 8th grid point).

is $512 \times 256 \times 256$ for x, y and z direction. This grid number is large enough for the two-points forcing inside the mixing-vane. The time increment is $0.0001t^*$, where t^* is the dimensionless time normalized by P/u_T. The SOR method for Eqs. (29) and (31) is carried out within 50 iterations, and then the error defined by Eq. (54) is confirmed to be approximately 10^{-5}. The computational result for the drag coefficient has been quantitatively verified in Ref. [17].

After the flow is developed, an instantaneous velocity field is picked up and shown in Fig. 25. Fig. 25a and b shows a separation above the mixing-vane containing large-scale fluctuation and a flow developing spatially along the strap after it is divided. The result suggests that the present method is applicable to such complex flows. Fig. 25c and d indicates that the velocity field around the mixing-vane, which is inclined from the coordinate axis, is captured reasonably by the present immersed boundary method. In Fig. 25d, the interflow from above and below the mixing-vane is reasonably simulated. The mixing-vane is very close to the rod surface, and then generating body fitted grid is difficult.

The lateral flows in the downstream of the spacer are shown in Fig. 26. The swirling flow shown in Fig. 26a is produced by the mixing-vane arrangement that has already shown in Fig. 24. On the other hand, as shown in Fig. 26b, a different mixing-vane arrangement can produce the cross flow to enhance the mixing between channels. The decay of these lateral flows has different mechanism [18], and it is important for flow control in the rod-bundle. In these computations, the mixing-vane arrangement is easily changed in the program by shuffling the interpolation coefficients for a mixing-vane.

5. Conclusion

A consistent scheme for immersed boundary method was developed to simulate the desired wall velocities precisely. The pressure field must maintain the consistency for the forcing velocity to represent the wall that does not coincide with the computational grid. For that purpose, a new wall condition for the pressure equation was introduced to equate the pressure gradient for the forcing velocity with that for the velocity used in the interpolation. This wall condition was incorporated into the velocity correction method and the pressure equation to compose the consistent scheme.

The conservation of wall condition in the present scheme was demonstrated theoretically. The momentum and energy conservations in the present scheme depended on the mass conservation. The present scheme was demonstrated to fulfill the mass conservation under the wall condition assured. These theoretical predictions were successfully verified by LES performed for plane channels aligned and inclined to the grid line.

With a view to unsteady turbulence simulation, temporal accuracy was analyzed using a generalized block LU decomposition. The result predicted that the temporal accuracy was decreased when one forcing velocity was used in the interpolation for another forcing. The LES result for the inclined channel indicated that the temporal accuracy was certainly decreased, and that the effect was however local at the forcing point and insignificant for global velocity field. This result is hopeful for the actual applications, where such overlapped forcing is inevitable.

The present scheme was successfully applied to LES of turbulent flow for complex geometries in Cartesian grid system. First, LES for a circular pipe was performed and the result was compared well with a DNS. This suggested that the present method was applicable to accurate unsteady turbulence simulation. Next, LES was performed for a nuclear rod-bundle that had complex three-dimensional configuration. The present immersed boundary method was advantageous for rearranging the configuration to optimize the flow control.

This study focused on the numerical scheme rather than the interpolation technique to improve the accuracy of the immersed boundary method. The present scheme was validated by both theoretical and numerical demonstrations. This validation improves the reliability and applicability of CFD on Cartesian grid system for the use of industrial interest, namely high Reynolds number flows in complex geometries.

References

[1] R. Mittal, G. Iaccarino, Immersed boundary methods, Annu. Rev. Fluid Mech. (2005) 239–260, doi:10.1146/annurev.fluid.373061903.175743.

[2] F.H. Harlow, J.E. Welch, Numerical calculation of time-dependent viscous incompressible flow of fluid with free surface, Phys. Fluids 8–12 (1965) 2182–2189.

[3] J. Mohd-Yusof, Combined immersed boundary/B-spline methods for simulations of flows in complex geometries, Center for Turbulence Research Annual Research Briefs (1997) 317–327.

[4] E.A. Fadlun, R. Verzicco, P. Orlandi, J. Mohd-Yusof, Combined immersed-boundary finite-difference methods for three-dimensional complex flow simulations, J. Comput. Phys. 161 (2000) 35–60, doi:10.1006/jcph.2000.6484.

[5] T. Ye, R. Mittal, H.S. Udaykumar, W. Shyy, An accurate Cartesian grid method for viscous incompressible flows with complex immersed boundaries, J. Comput. Phys. 156 (1999) 209–240, doi:10.1006/jcph.1999.6356.

[6] Y.H. Tseng, J.H. Ferziger, A goast-cell immersed boundary method for flow in complex geometry, J. Comput. Phys. 192 (2003) 593–623, doi:10.1016/jcph.2003.07.024.

[7] P.M. Gresho, Incompressible fluid dynamics: some fundamental formulation issues, Annu. Rev. Fluid Mech. 23 (1991) 413–453.

[8] J. Kim, D. Kim, H. Choi, An immersed-boundary finite-volume method for simulations of flow in complex geometries, J. Comput. Phys. 171 (2001) 132–150, doi:10.1006/jcph.2001.6778.

[9] J.B. Perot, An analysis of the fractional step method, J. Comput. Phys. 108 (1993) 51–58.

[10] T. Kajishima, Conservation properties of finite difference method for convection, Trans. Jpn Soc. Mech. Eng. Ser. B 60 (574) (1994) 2058–2063 (in Japanese).

[11] J. Kim, P. Moin, Application of a fractional step method to incompressible Navier–Stokes equations, J. Comput. Phys. 59 (1985) 308–323.

[12] J.K. Dukowics, A.S. Dvinsky, Approximate factorization as a high order splitting for the implicit incompressible flow equations, J. Comput. Phys. 102 (1992) 336–347.

[13] K. Yokoi, Numerical method for a moving solid object in flows, Phys. Rev. E67 (2003) 045701-1–045701-4.

[14] Y. Morinishi, T.S. Lund, O.V. Vasilyev, P. Moin, Fully conservative higher order finite difference schemes for incompressible flow, J. Comput. Phys. 143 (1998) 90–124.

[15] J.G.M. Eggels, F. Unger, M.H. Weiss, J. Westerweel, R.J. Adrian, R. Friedrich, F.T.M. Nieuwstadt, Fully Developed Turbulent Pipe Flow: a Comparison between Direct Numerical Simulation and Experiment, J. Fluid. Mech. 268 (1994) 175–209.

[16] T. Kajishima, T. Nomachi, One-equation subgrid scale model using dynamic procedure for the energy production, Trans ASME J. Appl. Mech. 73 (3) (2006) 368–373.

[17] T. Ikeno, T. Kajishima, Decay of Swirling Turbulent Flow in Rod-bundle, J. Fluid Sci. Technol. 1 (1) (2006) 36–47.

[18] T. Ikeno, T. Kajishima, T. Murata, The effect of mixing-vane arrangements in a subchannel turbulent flow, J. Nucl. Sci. Technol. 43 (10) (2006) 1194–1205.